Chemical Science

ROYAL SOCIETY OF CHEMISTRY

EDGE ARTICLE

View Article Online
View Journal | View Issue

Cite this: *Chem. Sci.*, 2025, **16**, 3611

All publication charges for this article have been paid for by the Royal Society of Chemistry

Received 28th September 2024
Accepted 21st January 2025

DOI: 10.1039/d4sc06578f

rsc.li/chemical-science

Precise photorelease in living cells by high-viscosity activatable coumarin-based photocages†

Xinyi Huang,‡[a] Yajie Shi,‡[b] Li Jiang,*[a] Wanqi Chen,[a] Bingkun Bao,[a] Tuan Liu,[a] Qinghai Zhou,[c] Jiaxin Li,[a] Qiuning Lin *[a] and Linyong Zhu[a]

Intracellular viscosity is a critical microenvironmental factor in various biological systems, and its abnormal increase is closely linked to the progression of many diseases. Therefore, precisely controlling the release of bioactive molecules in high-viscosity regions is vital for understanding disease mechanisms and advancing their diagnosis and treatment. However, viscosity alone cannot directly trigger chemical reactions. Inspired by molecular rotor fluorophores, we have developed a series of high-viscosity activated photocages by modifying the C3 position of the coumarin scaffold with electron-withdrawing groups. In low-viscosity environments, both fluorescence and photocleavage of the photocages are inhibited by nonradiative decay caused by intramolecular free rotation. In contrast, in high-viscosity environments, the restriction of this intramolecular rotation restores fluorescence and photocleavage. These unique photolysis properties enable the selective photorelease of these photocages in high-viscosity conditions. As a proof of concept, we have developed a drug delivery system that targets abnormal mitochondria with high viscosity. This system demonstrates enhanced photolysis efficiency in abnormal mitochondria compared to normal ones, allowing for precise drug release in diseased mitochondria while ensuring excellent biological safety in healthy mitochondria. We anticipate that these photocages will serve as convenient and efficient tools for the precise release of active molecules in high-viscosity environments.

Introduction

Viscosity is a critical parameter in the microenvironment of cells, tissues, and organs, with its distribution varying across different regions.[1,2] It directly affects the diffusion rates of molecular species and the reaction rates of diffusion-controlled processes, thereby playing a key role in maintaining normal cellular functions.[2] Abnormally high viscosity levels, both at the cellular and organismal levels, have been linked to several dysfunctions and diseases, including atherosclerosis,[3] diabetes,[4] Alzheimer's disease[5] and cancer.[6] Therefore, developing viscosity as a stimulus for the precise control and release of bioactive molecules, such as drugs, in high-viscosity regions is crucial for understanding disease mechanisms, as well as for their diagnosis and treatment. Unfortunately, unlike pH and redox signals, viscosity, as an inherent internal stimulus, cannot directly trigger chemical reactions.[7,8]

Photocages, which are light-sensitive chemical protecting groups, are widely used to design light-mediated controlled release systems with high spatio-temporal resolution.[9–17] Traditional photocages are typically based on *o*-nitrobenzyl,[18] benzoinyl (desyl)[19] and coumarin,[20] all of which exhibit short absorption wavelengths. In recent years, significant efforts have focused on developing photocages activated by visible and near-infrared light, utilizing coumarin,[21–24] BODIPY,[25] and cyanine[26,27] to enhance tissue light penetration. Furthermore, novel photocages, including organic/metal hybrid based-photocages[14,17] and fluorogen-based photocages,[15,16] have been developed, increasing versatility in chemical and biological systems while extending absorption wavelengths of photocages. Simultaneously, conditionally activatable photocages have also been developed (Table S1†). These photocages remain unresponsive to light under normal conditions but become photoactivatable in the presence of specific stimuli. Conditionally activatable photocages offer enhanced control and precision in cargo release due to their incorporation of dual orthogonal stimuli. Our group was the first to validate this concept by developing target-activated coumarin photocages locked by maleimide moieties.[28,29] The reaction between disulfide bond and thiol groups unlocks the coumarin photocage, allowing for

[a]*School of Biomedical Engineering, Shanghai Jiao Tong University, Shanghai 200240, China. E-mail: qiuninglin@sjtu.edu.cn*

[b]*Optogenetics & Synthetic Biology Interdisciplinary Research Center, State Key Laboratory of Bioreactor Engineering, East China University of Science and Technology, Shanghai 200237, China*

[c]*The Education Ministry Key Lab of Resource Chemistry, Joint International Research Laboratory of Resource Chemistry of Ministry of Education, Shanghai Key Laboratory of Rare Earth Functional Materials, Shanghai Frontiers Science Center of Biomimetic Catalysis, College of Chemistry and Materials Science, Shanghai Normal University, Shanghai 200234, China*

† Electronic supplementary information (ESI) available. See DOI: https://doi.org/10.1039/d4sc06578f

‡ These authors contributed equally to this work.

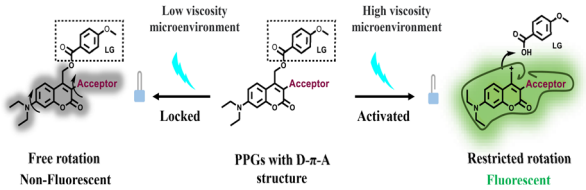

Scheme 1 Schematic representation of HVP based on coumarin, modified with an electron-withdrawing group at C3 position.

subsequent cargo release upon light irradiation. Nitroimidazole and methotrexate have also been used to lock photocages, which are then unlocked in hypoxic environments or in the presence of DT-diaphorase enzymes, facilitating cargo release under light stimulation.[30,31] Recently, Kele *et al.* reported a clickable coumarin photocage locked by tetrazine moieties, which was unlocked following the reaction between tetrazine and BCN.[32]

In this study, we present the development of a series of novel high-viscosity activatable photocages (HVP) designed for the precise release of active molecules in high-viscosity environments (Scheme 1). Our design leverages the intrinsic photo-S_N1-dependent cleavage of coumarin photocages,[33,34] incorporating elements from molecular rotor fluorophores, whose energy deactivation in the S_1 state is tightly regulated by viscosity.[35–37] In low-viscosity environments (locked state), photoexcitation of the HVP leads to relaxation *via* the twisted intramolecular charge transfer (TICT) state,[38,39] effectively suppressing both coumarin fluorescence and photocleavage. In contrast, in high-viscosity environments (unlocked state), the HVP become reactivated, restoring fluorescence and releasing the caged compounds upon exposure to visible light. Using chlorambucil as a model drug, we developed a drug delivery system specifically designed to release the drug in abnormal mitochondria, which are characterized by high viscosity. This system demonstrated enhanced cytotoxicity in cells with abnormal mitochondria while maintaining biological safety in normal cells. The exceptional photolysis performance of the developed HVP suggests their potential in applications requiring precise control of molecular release.

Results and discussion

Molecular design and characterization

Structurally, molecular rotor fluorophores contain a "push–pull" system, which includes an electron donor, an electron acceptor, and π-conjugation that facilitate charge transfer (D–π–A).[40] These fluorophores typically feature a single C–C bond between the π-conjugation and the acceptor, which has a low intrinsic rotational barrier. This property has been exploited to create fluorophores with fluorescence intensity that is sensitive to change in solvent viscosity.[41] Inspired by the chromophore structure of molecular rotor fluorophores, we envisaged that developing HVP would be achieved by direct introduction of electron-withdrawing groups at the C3 position of the 7-(Diethylamino)coumarin (DEAC), linking with a rotational C–C single bond (Fig. 1A and Scheme S1†).

To test our hypothesis, we introduced pyridine salt and cyano groups with varying electron-withdrawing capacities (EWC) at the C3 position of DEAC, producing compounds CBA and CBA1. CBA exhibited a redshifted absorption wavelength compared to CBA1, which can be attributed to the increased EWC of the electron-withdrawing group (Fig. 1B). Additionally, the photo-S_N1 cleavage mechanism suggested that the deactivation pathways of coumarin photocages in the S_1 state are influenced by a synergistic effect of photochemical reactions and fluorescence (Fig. S1†). To assess the viscosity sensitivity of the photocages, we performed fluorescence measurements in solvents with differing viscosities and polarities. Both CBA and CBA1 exhibited a weak response to solvent polarity, while demonstrating a strong response to solvent viscosity (Fig. 1C, S2 and S3†). The highest fluorescence intensity of CBA and CBA1 was observed in glycerol, despite the presence of slight spectral migration in solvents of varying polarities. In solvents with different viscosities, CBA exhibited greater sensitivity to heightened viscosity relative to CBA1 (Fig. 1D). The fluorescence quantum yield of CBA and CBA1, in methanol (1.92% for CBA, 11.97% for CBA1) and glycerol (22.59% for CBA, 44.10% for CBA1) support these findings (Table S2†). By fitting the Förster–Hoffmann equation, we found that CBA had higher viscosity sensitivity than CBA1, with a sensitivity coefficient of 0.62, comparable to the classical molecular rotor-based fluorophore CCVJ (Fig. S3D†).[42] These results confirm that modifying the C3 position of the coumarin scaffold with electron-withdrawing groups is an effective strategy for developing HVP.

To further investigate the effect of the EWC of CBA and CBA1 on photolytic behavior, we conducted photolysis experiments in solvents with varying viscosities (Table S3†). Prior to the photolysis experiments, we tested the storage stability of the compounds, confirming that the photocages remained stable in a dark environment (Fig. S4†). All compounds (3×10^{-4} M) were irradiated using an LED light source at 450 nm with a light intensity of 10 mW cm^{-2}. In glycerol, CBA demonstrated higher photolysis efficiency compared to CBA1, which aligned with the EWC order of the substituent groups (CBA > CBA1) (Fig. 1E and Table 1). However, in methanol, the photolysis efficiency was reversed, with CBA1 exhibiting greater efficiency than CBA (Fig. 1F and Table 1). This trend was consistent with the fluorescence data. Notably, CBA and CBA1 exhibited a gradual release of cargo as solvent viscosity increased from methanol to glycerol, verified by reverse-phase HPLC (Fig. 1G, S5 and S6†). Consequently, CBA achieved the highest photolysis efficiency in glycerol, attaining full photolytic conversion after just 18 minutes, and a photochemical quantum yield of 1.646% (Fig. 1H). The photochemical quantum yield of CBA in glycerol was 274-fold higher than in methanol (Fig. 1I). Utilizing CBA's high viscosity sensitivity, we were able to control its photolysis in an "on-and-off" manner (Fig. S7†).

We next attempted to extend the absorption wavelengths of the photocages *via* structural modifications. Drawing on Kele's research,[43] we introduced a conjugated double bond between the coumarin scaffold and the electron-withdrawing pyridine salt of CBA, producing CBA2 (Fig. 1A). Based on the same modification method, compound CBA3 was obtained from

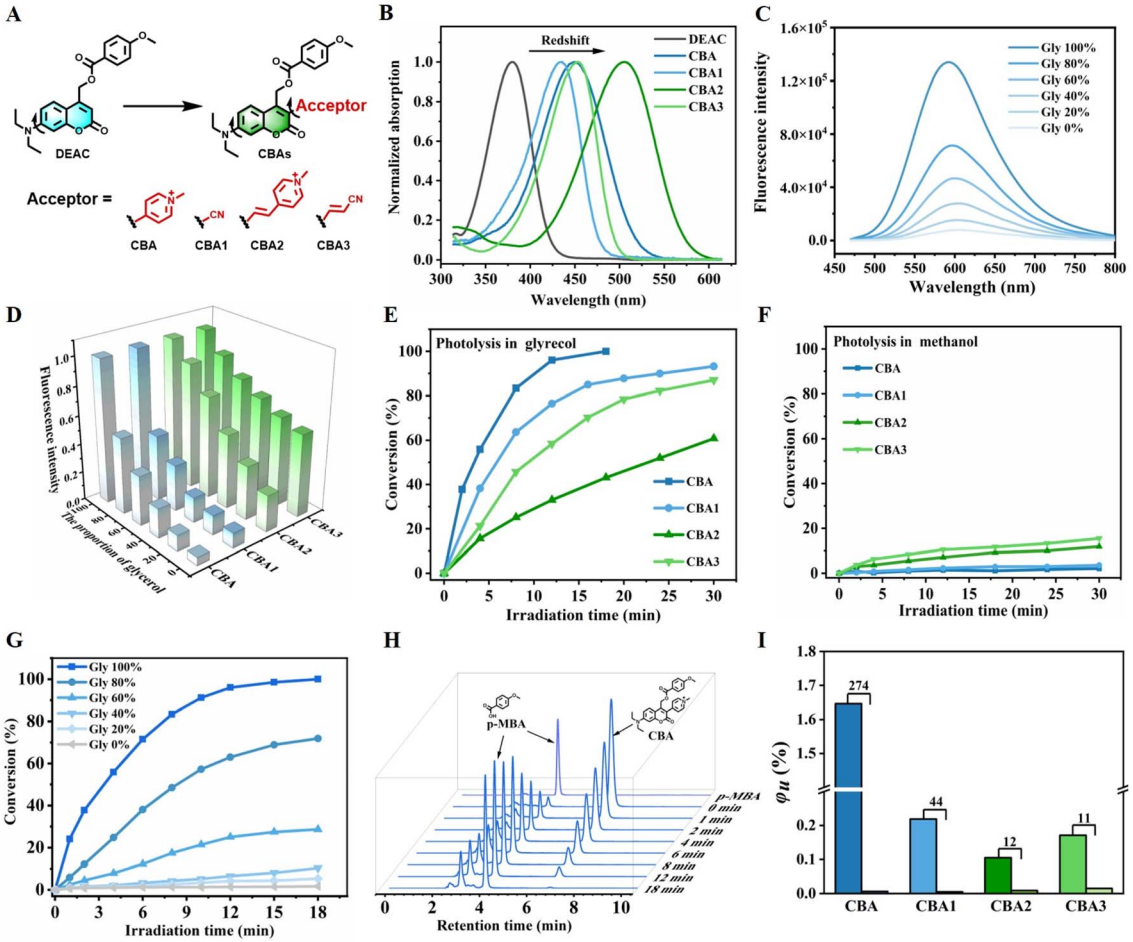

Fig. 1 (A) Chemical structures of DEAC, CBA, and CBA1-CBA3. (B) Normalized absorbance spectra of DEAC, CBA, and CBA1-CBA3 in methanol. (C) Fluorescent intensities of CBA in a mixed solution of methanol and glycerol of different ratios (glycerol/methanol = 0%, 20%, 40%, 60%, 80%, and 100%). The concentrations of tested samples are 10 μM. (D) Normalized fluorescent intensities of CBA and CBA1-CBA3 in a mixed solution of methanol and glycerol of different ratios (glycerol/methanol = 0%, 20%, 40%, 60%, 80%, and 100%). (E) Photolysis conversion *vs.* irradiation times of CBA and CBA1-CBA3 in glycerol. (F) Photolysis conversion *vs.* irradiation times of CBA and CBA1-CBA3 in methanol. (G) Photolytic conversion *vs.* irradiation times of CBA in a mixed solution of methanol and glycerol with different ratios (glycerol/methanol = 0%, 20%, 40%, 60%, 80%, and 100%). (H) Photolysis of CBA in glycerol assessed by reverse-phase HPLC. (I) The ratio of photochemical quantum yields of CBA and CBA1-CBA3 in glycerol *vs.* methanol. Photolysis conditions: all tested samples (3×10^{-4} M) were irradiated by LED light sources at 450 nm (CBA, CBA1, and CBA3) and 520 nm (CBA2), with the light intensity of 10 mW cm^{-2}.

CBA1. As expected, CBA2 and CBA3 exhibited redshifted absorption wavelengths compared to CBA and CBA1, with the maximum absorption wavelength of CBA2 exceeding 500 nm (Fig. 1B). These results can be attributed to the extension of the π-conjugated system. However, CBA2 and CBA3 demonstrated lower photolytic efficiency in glycerol than CBA and CBA1

Table 1 Photophysical and photochemical features of compounds

Photocages[a]	λ_{max}[b] (nm)	ε_{max} (M^{-1} cm^{-1})	φ_{u1} (%) in glycerol	φ_{u2} (%) in methanol	$\varepsilon_{max}\varphi_{u1}$ (M^{-1} cm^{-1}) in glycerol	$\varepsilon_{max}\varphi_{u2}$ (M^{-1} cm^{-1}) in methanol	Ratio $\varphi_{u1}/\varphi_{u2}$
CBA	**450**	**21 486**	**1.646**	**0.006**	**353.7**	**1.3**	**274**
CBA1	436	40 728	0.219	0.005	89.2	2.0	44
CBA2	506	34 788	0.105	0.009	36.5	3.1	12
CBA3	454	29 720	0.171	0.015	50.8	4.5	11
DEAC	380	22 522	1.121	0.683	252.5	153.1	2

[a] The leaving group is *p*-methoxybenzoic acid. [b] Symbols and abbreviations: λ_{max}, absorption maximum (nm); ε_{max}, molar extinction coefficient (M^{-1} cm^{-1}); φ_{u1}, photochemical quantum yield in glycerol; φ_{u2}, photochemical quantum yield in methanol; $\varepsilon_{max}\varphi_{u1}$, photolysis efficiency in glycerol (M^{-1} cm^{-1}); $\varepsilon_{max}\varphi_{u2}$, photolysis efficiency in methanol (M^{-1} cm^{-1}). The photochemical quantum yields were determined using potassium ferrioxalate as an actinometer.

(Fig. 1E). This reduction in efficiency may result from lowered viscosity sensitivity of CBA2 and CBA3 compared to CBA and CBA1, as both CBA2 and CBA3 exhibited weaker viscosity responsiveness in fluorescence (Fig. 1D, S2 and S3†). The fluorescence spectra of CBA3 exhibited noticeable polarity-dependent band shifts in solvents of differing polarities, aligning with its lowest viscosity sensitivity coefficient (Fig. S2D and S3E†). These results demonstrated the incorporations of vinyl can significantly extend the wavelengths of the photocages, but have adverse effects on viscosity sensitivity. The direct linkage between the electron-withdrawing groups and coumarins at the C3 position *via* a rotatable single bond is a more effective strategy to increase the viscosity sensitivity of photocages.

Photolysis mechanism of CBAs

The TICT is a well-known energy transduction mechanism in molecular rotor fluorophores.[38] During TICT, a fluorophore undergoes intramolecular free rotations that consume energy, facilitating the transition of compounds into the TICT state under low-viscosity conditions. This transition results in fluorescence quenching. In contrast, under high-viscosity conditions, the restriction of intramolecular rotations limits the transition into the TICT state, leading to enhanced fluorescence (Fig. S8†). To investigate the relationship between the photolysis mechanism and the TICT state, we performed theoretical calculations on CBA and CBA1, using DEAC as a control. Density functional theory (DFT) calculations for molecular geometry optimization revealed that DEAC had a significant redistribution of electrons from the highest occupied molecular orbital (HOMO) to the lowest unoccupied molecular orbital (LUMO), resulting in an energy gap of 3.88 eV. This finding indicates a strong intramolecular charge transfer (ICT) transition in its excited state (Fig. 2A). In contrast, CBA (2.46 eV) and CBA1 (3.58 eV) showed lower energy gaps compared to DEAC, suggesting that the electron-withdrawing groups at the C3 position of coumarin have a stronger stabilizing effect on both the LUMO and HOMO (Fig. 2A). This stabilization reduces the energy gap for de-excitation during emission, leading to a spectral redshift. This observation is consistent with the fact that CBA and CBA1 exhibit longer λ_{max} values than DEAC (Fig. 1B).

We further performed time-dependent density functional theory (TD-DFT) calculations to investigate the mechanism underlying the viscosity sensitivity of CBA and CBA1. The energy barrier (ΔE) between the locally excited state and the TICT state serves as an indicator of viscosity sensitivity, as used in previous studies on molecular rotors (Fig. S8†).[44] DEAC showed a high energy barrier ($\Delta E = 12.4$ kcal mol^{-1}) for transitioning from the locally excited state to the TICT state (Fig. 2B). This high ΔE value suggests that the transition of DEAC to the TICT state is challenging, which aligns with its high photochemical quantum yield in methanol (Table 1). In contrast, CBA and CBA1 exhibited ΔE values of 5.1 and 0.3 kcal mol^{-1}, respectively (Fig. 2C and D). These lower ΔE values indicate that CBA and CBA1 transition to the TICT state more readily than DEAC. Consequently, CBA and CBA1 display greater viscosity

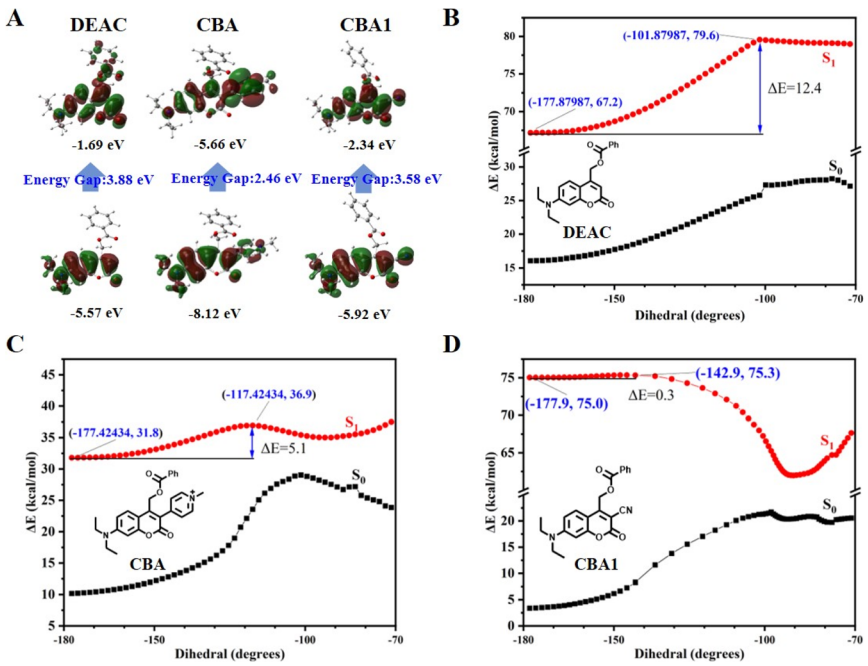

Fig. 2 (A) HOMO and LUMO orbitals of DEAC, CBA, and CBA1. Calculated HOMO–LUMO energy levels and de-excitation energies (energy gap) of DEAC, CBA, and CBA1, respectively. (B) Potential energy surfaces of DEAC at the S_1 and S_0 states. (C) Potential energy surfaces of CBA at the S_1 and S_0 states. (D) Potential energy surfaces of CBA1 at the S_1 and S_0 states. Note: To save resources and computational costs, the leaving groups DEAC, CBA, and CBA1 are simplified to benzene. ΔE represents the energy barrier between the locally excited state and the TICT state and has been used to assess the viscosity sensitivity of molecular rotors in previous studies.

sensitivity compared to DEAC. Moreover, CBA1 had a lower ΔE than CBA, suggesting that CBA1 requires a higher viscosity to restrict the energy dissipation caused by molecular rotation.[45] This finding is consistent with the higher photolysis efficiency of CBA compared to CBA1 in glycerol (Fig. 1E). Based on these calculations, we conclude that the high viscosity sensitivity of CBA and CBA1 is attributable to the TICT mechanism which is similar to molecular rotor fluorophores.

Targeting mitochondria in living cells

Mitochondria are central to cellular metabolism and play crucial roles in physiological processes such as cellular growth, differentiation, and apoptosis, thereby regulating cell functions.[46] Mitochondrial viscosity affects mitochondrial protein regulation, respiratory status, and signal transduction, and is closely related to mitochondrial function. Abnormal changes in mitochondrial viscosity can impair cell function, accelerate aging, and contribute to diseases such as Parkinson's disease, diabetes, cardiac disease, and fatty liver.[47] Consequently, targeting abnormal mitochondria is important for understanding disease mechanisms, as well as for diagnosing and treating these diseases. Cationic salt probes are often designed to target mitochondria due to the negative potential of the mitochondrial membrane.[48] Given CBA's high viscosity sensitivity and its cationic structure, we hypothesized that CBA could serve as a targeting moiety for mitochondrial localization.[49,50] To test this, we investigated CBA's ability to target abnormal mitochondria in living cells. We created an abnormal mitochondria model by treating mitochondria with monensin (Mon), a drug known to induce mitochondrial dysfunction and increase mitochondrial viscosity.[51] Untreated mitochondria served as controls for comparison.

Cell membrane permeability is crucial for intracellular applications. To investigate the ability of CBA to penetrate cell membranes, we incubated HeLa cells with CBA. Fluorescence was detectable within the HeLa cells, indicating that CBA successfully penetrated the cell membrane (Fig. 3A). To determine the localization of CBA within the cells, we conducted colocalization experiments using a commercially available mitochondrial dye, MitoTracker Deep Red FM. CBA exhibited fluorescence in the green channel (ex = 450 nm, em = 470–625 nm), while MitoTracker Deep Red FM stained the mitochondria and appeared in the red channel (ex = 644 nm, em = 655–720 nm) (Fig. 3A). The merged image demonstrated a strong correlation between CBA staining and the mitochondrial tracker. Intensity profiles from linear regions of interest in HeLa cells co-stained with CBA and MitoTracker Deep Red FM showed similar patterns (Fig. 3C and D). Pearson's coefficients for the overlap of CBA and MitoTracker Deep Red FM were calculated as 0.91 for abnormal mitochondria and 0.85 for normal mitochondria. These results confirm that CBA can specifically target and localize in mitochondria.

To investigate CBA's ability to recognize abnormal mitochondria in living cells, we evaluated the fluorescence intensities of CBA in abnormal and normal mitochondria. The fluorescence intensity of CBA increased with concentration in both types of mitochondria, attributable to CBA's cationic

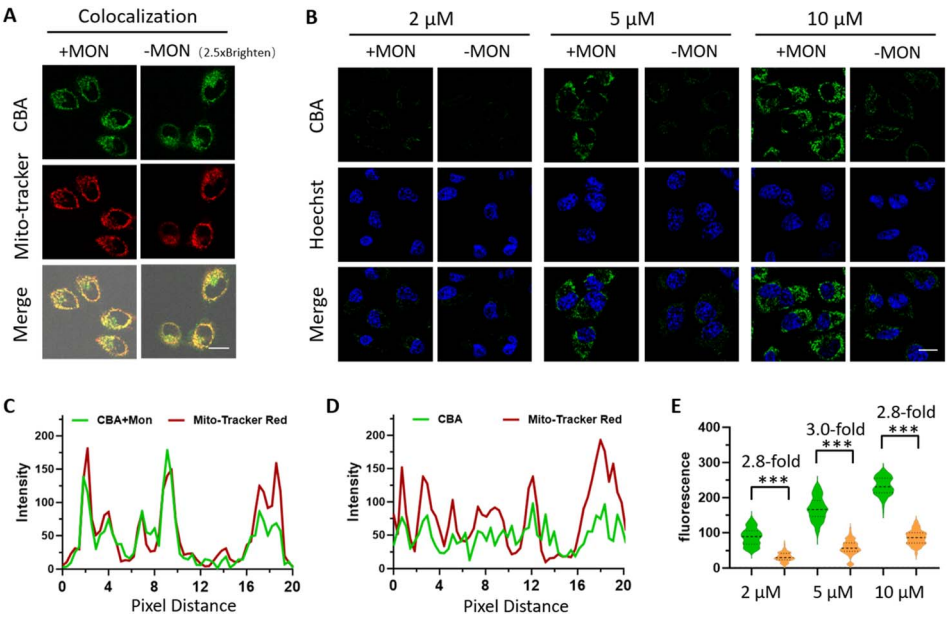

Fig. 3 (A) Representative confocal images of live HeLa cells with or without Mon treatment incubated with 10 μM CBA and 1 μM MitoTracker Deep Red FM. CLSM images were collected *via* the green channel (ex = 450 nm, em = 470–625 nm) and the red channel (ex = 644 nm, em = 655–720 nm). (B) Representative confocal images of live HeLa cells with or without Mon treatment incubated with 0.5 μg mL^{-1} Hoechst 33 342 and different concentrations of CBA. CLSM images were collected *via* the blue channel (ex = 405 nm, em = 415–440 nm) and the green channel (ex = 450 nm, em = 470–625 nm). (C) Intensity profile of CBA and MitoTracker Deep Red FM in Mon treated HeLa cells. (D) Intensity profile of CBA and MitoTracker Deep Red FM in untreated HeLa cells. (E) Fluorescence intensities of cells in 3(B). Statistical comparisons were performed by a two-tailed *t*-test. ***$P < 0.001$. Data represent the mean ± SD ($N \geq 90$ cells). Scale bars, 20 μm.

structure, which targets mitochondria, leading to its accumulation and enhanced fluorescence. However, the fluorescence intensity of CBA in normal mitochondria was lower, even at a high concentration of 10 μM (Fig. 3B and E). The fluorescence intensity of CBA in abnormal mitochondria was approximately three times higher than in normal mitochondria (Fig. 3E). In methanol, the addition of Mon to CBA did not result in increased fluorescence, indicating that the fluorescence enhancement in cells was due to increased mitochondrial viscosity (Fig. S9†). These findings suggest that the high viscosity of abnormal mitochondria restricts the molecular rotation of CBA, thereby enhancing its fluorescence. In contrast, the viscosity of normal mitochondria does not significantly restrict CBA's molecular rotation, resulting in weaker fluorescence. Consequently, CBA specifically recognizes abnormal mitochondria, demonstrating its potential for diagnosing diseases associated with high viscosity.

Drug release in abnormal mitochondria

Based on the high viscosity sensitivity and abnormal mitochondrial localization of CBA, we used CBA to construct a drug delivery system. Chlorambucil (CL), an anti-cancer agent, has been shown to exert cytotoxic effects by depolarizing the

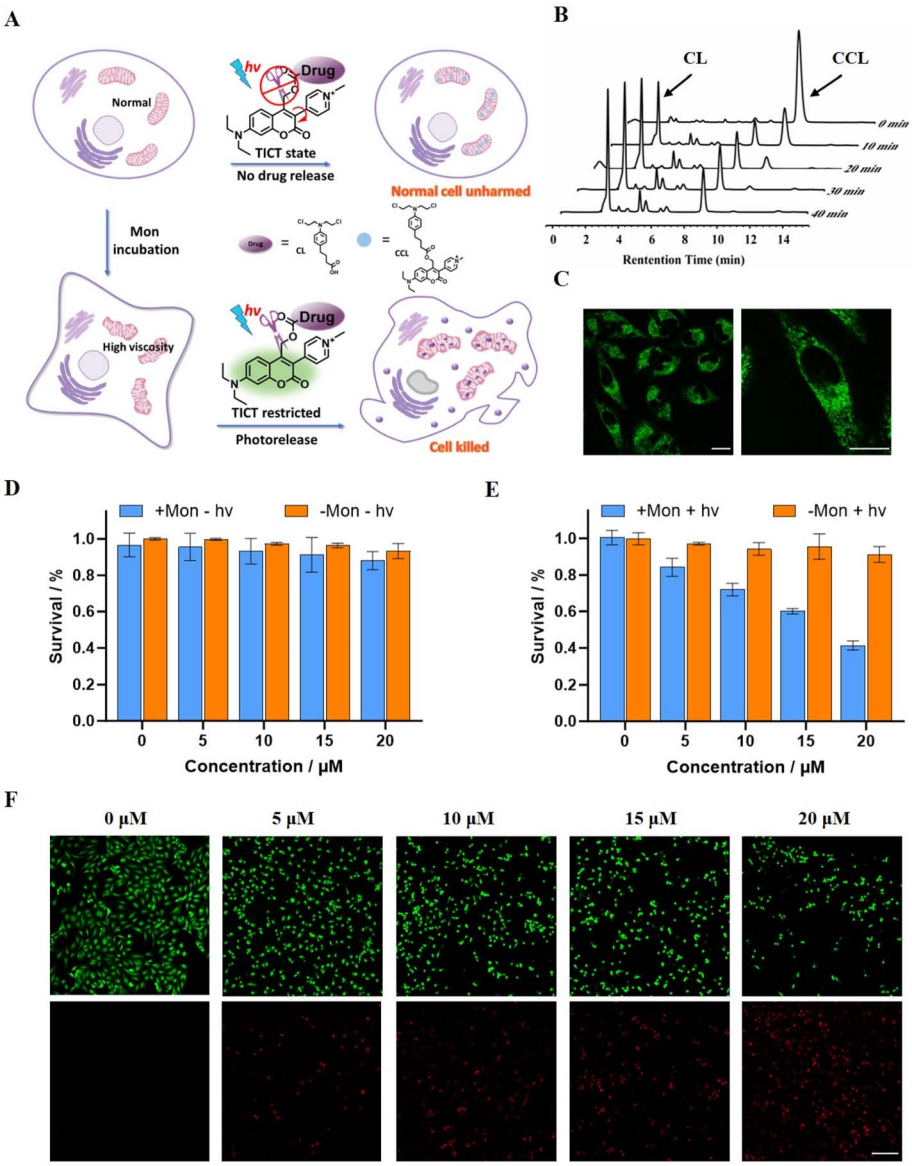

Fig. 4 (A) Schematic representation of the high-viscosity activatable drug release system of CCL. (B) Photolysis of CCL in glycerol assessed by reverse-phase HPLC. Photolysis conditions: the tested sample (3×10^{-4} M) was irradiated by a LED light source at 450 nm, with a light intensity of 50 mW cm^{-2}. (C) Representative confocal images of HeLa cells with 10 μM CCL. Scale bars, 30 μm. (D) Cell viability of HeLa cells incubated with 0–20 μM CCL in the dark with (blue) or without (orange) Mon treatment. (E) Cell viability of HeLa cells incubated with 0–20 μM CCL under 15 minutes of light irradiation (440–450 nm, 15 mW cm^{-2}) with (blue) or without (orange) Mon treatment. (F) Representative images of live/dead staining of Mon-treated HeLa cells (green: live cells, red: dead cells) incubated with different doses of CCL, irradiated for 15 minutes (440–450 nm, 15 mW cm^{-2}) and cultured for 48 hours. Scale bar, 200 μm.

mitochondrial membrane potential, increasing reactive oxygen species (ROS), and damaging mitochondrial DNA (mtDNA). [52–54] Therefore, we attached CL to CBA to develop a drug delivery system, which we termed CCL (Fig. 4A and Scheme S6†). We monitored the drug release behavior of CCL *in vitro* using reverse-phase HPLC. In glycerol, CL release increased with longer irradiation times, and we identified complete CL release from CCL in 40 minutes under a 450 nm LED light source with a light intensity of 50 mW cm^{-2} (Fig. 4B). In contrast, we observed negligible CL release in methanol (Fig. S10A†). Additionally, the fluorescence intensity of CCL increased with the proportion of glycerol (Fig. S10B†). Fluorescence signals in HeLa cells demonstrated that CCL can penetrate cell membranes and specifically localize in mitochondria (Fig. 4C). These results show that modifying CBA with CL does not significantly impact its viscosity sensitivity or mitochondria-targeting capability.

We treated HeLa cells with Mon to produce a high viscosity level in the mitochondria and incubated them with CCL. We evaluated the high-viscosity activatable photolysis property of CCL by measuring the survival rate of HeLa cells using the CCK8 assay. Untreated HeLa cells served as the control. In the absence of light irradiation, the addition of CCL did not affect the survival rate of HeLa cells, regardless of Mon treatment, demonstrating the desired biosafety of CCL (Fig. 4D). Upon exposure to light from a 96-well plate-adapted light source (Fig. S11†), the survival rate of HeLa cells decreased as the concentration of CCL increased. When the concentration of CCL is 20 μM, approximately 40% of Mon-treated HeLa cells survived (Fig. 4E and S12†). Conversely, in the absence of Mon treatment, the survival rate of HeLa cells at a CCL concentration of 20 μM was approximately 85%, over twice that of HeLa cells treated with Mon. The CCK8 assay demonstrated that CCL exhibited an IC_{50} of 15.55 μM in cells with abnormal mitochondria, whereas the IC_{50} in cells with normal mitochondria was 40.28 μM (Fig. S12†). In addition, CBA and CL exhibited negligible cytotoxicity regardless of exposure to light or darkness, and irrespective of treatment with Mon. This finding confirmed that cell death resulted from CL released from CCL rather than the illumination or photolysis process. Results from the live-dead cell staining experiment were consistent with the CCK8 assay results (Fig. 4F and S13†). The higher drug efficacy of CCL in abnormal mitochondria compared to normal mitochondria suggests that CCL effectively targets lesions with abnormal high viscosity. The lower toxicity of CCL in normal mitochondria indicates fewer side effects in normal regions. This study represents the first instance to use high viscosity as a stimulus to activate photocages for achieving precisely controlled release of cargo.

Conclusions

In this study, we developed a series of HVP by introducing electron-withdrawing groups at the C3 position of the coumarin scaffold. These photocages showed remarkable viscosity-dependent photolysis, with low photolysis efficiency in low-viscosity environments and high efficiency in high-viscosity conditions. Theoretical calculations revealed that the electron-withdrawing groups at the C3 position reduce the energy barrier for transitioning from the LE state to the TICT state *via* intramolecular rotations, thereby increasing viscosity sensitivity. Among the compounds synthesized, CBA exhibited the highest sensitivity to viscosity, with a photochemical quantum yield of 0.006% in methanol and 1.646% in glycerol, representing a 274-fold increase. Additionally, CBA specifically targeted abnormal mitochondria in HeLa cells without requiring further modifications to the targeting reagent. Building on these findings, we developed a drug delivery system (CCL) incorporating CBA for targeted mitochondrial drug release. CCL demonstrated superior photolysis efficiency in abnormal mitochondria with high viscosity compared to normal mitochondria, resulting in enhanced drug release and selective elimination of cells with abnormal mitochondria while ensuring biosafety in cells with normal mitochondria. Overall, our novel HVP provide a powerful approach for areas requiring precise and controlled release of active molecules.

Data availability

The data supporting this article have been included as part of the ESI.†

Author contributions

Qiuning Lin and Linyong Zhu conceived of the ideas. Xinyi Huang, Yajie Shi, and Li Jiang were responsible for the experimental concept, design, and data analysis. Li Jiang, Xinyi Huang, Yajie Shi wrote the manuscript. Qinghai Zhou performed theoretical calculations. Xinyi Huang, Yajie Shi, Li Jiang, and Jiaxin Li synthesized, characterized the molecule, and analyzed the data. Xinyi Huang, Wanqi Chen, Bingkun Bao, and Tuan Liu evaluated the cytotoxicity and biocompatibility of the photocages. Qiuning Lin and Linyong Zhu provided financial support and supervised this work. All authors commented on the manuscript and its revisions.

Conflicts of interest

There are no conflicts to declare.

Acknowledgements

This work was financially supported by the 173 Plan Project (2019-JCJQ-ZD-359-00), the National Natural Science Foundation of China (32121005 and 22475129), the Interdisciplinary Program of Shanghai Jiao Tong University (YG2022ZD009 and YG2024QNA19), the China Postdoctoral Science Foundation (2023M742278 and 2024T170560), and the Postdoctoral Fellowship Program of CPSF (GZC20231603).

Notes and references

1 S. Park, W.-H. Jung, M. Pittman, J. Chen and Y. Chen, *J. Biomech. Eng.*, 2020, **142**, 100804.

2 S. Wang, W. X. Ren, J.-T. Hou, M. Won, J. An, X. Chen, J. Shu and J. S. Kim, *Chem. Soc. Rev.*, 2021, **50**, 8887–8902.
3 Z. Wang, S. Wang, B. Wang, J. Shen, L. Zhao, F. Yu and J.-T. Hou, *Chem. Eng. J.*, 2023, **464**, 142687.
4 J. Zhang, S. Gong, Y. Liu, Z. Zheng and G. Feng, *Sens. Actuators, B*, 2024, **406**, 135432.
5 W. Wu, L. Zhao, Y. Zhang, J. Wei, J. Han, Y. Zhang and Z. Zhao, *Sci. Rep.*, 2024, **14**, 1336.
6 K. Bera, A. Kiepas, I. Godet, Y. Li, P. Mehta, B. Ifemembi, C. D. Paul, A. Sen, S. A. Serra, K. Stoletov, J. Tao, G. Shatkin, S. J. Lee, Y. Zhang, A. Boen, P. Mistriotis, D. M. Gilkes, J. D. Lewis, C.-M. Fan, A. P. Feinberg, M. A. Valverde, S. X. Sun and K. Konstantopoulos, *Nature*, 2022, **611**, 365–373.
7 H. U. Kim, D. G. Choi, Y. H. Roh, M. S. Shim and K. W. Bong, *Small*, 2016, **12**, 3463–3470.
8 R. Xia, Q. Pei, J. Wang, Z. Wang, X. Hu and Z. Xie, *J. Colloid Interface Sci.*, 2020, **580**, 785–793.
9 K.-Y. Chung, A. Uddin and Z. A. Page, *Chem. Sci.*, 2023, **14**, 10736–10743.
10 P. Klán, T. Šolomek, C. G. Bochet, A. Blanc, R. Givens, M. Rubina, V. Popik, A. Kostikov and J. Wirz, *Chem. Rev.*, 2013, **113**, 119–191.
11 R. Weinstain, T. Slanina, D. Kand and P. Klán, *Chem. Rev.*, 2020, **120**, 13135–13272.
12 T. Liu, B. Bao, Y. Li, Q. Lin and L. Zhu, *Prog. Polym. Sci.*, 2023, **146**, 101741.
13 I. Aujard, C. Benbrahim, M. Gouget, O. Ruel, J. B. Baudin, P. Neveu and L. Jullien, *Chem.–Eur. J.*, 2006, **12**, 6865–6879.
14 A. R. Sekhar, Y. Chitose, J. Janoš, S. I. Dangoor, A. Ramundo, R. Satchi-Fainaro, P. Slavíček, P. Klán and R. Weinstain, *Nat. Commun.*, 2022, **13**, 3614.
15 S. Mondal, W. L. Koay, I. Daga, S. Paul, V. X. Truong and N. D. P. Singh, *J. Am. Chem. Soc.*, 2024, **146**, 23376–23386.
16 S. Mondal, A. Chatterjee, S. Banerjee, T. Singha, A. Sikder, T. K. Bhattacharyya, M. Mandal, P. K. Datta, T. K. Maiti and N. D. P. Singh, *ACS Appl. Mater. Interfaces*, 2023, **15**, 32099–32109.
17 M. He, G. He, P. Wang, S. Jiang, Z. Jiao, D. Xi, P. Miao, X. Leng, Z. Wei, Y. Li, Y. Yang, R. Wang, J. Du, J. Fan, W. Sun and X. Peng, *Adv. Sci.*, 2021, **8**, 2103334.
18 M. Abe, Y. Chitose, S. Jakkampudi, P. Thuy, Q. Lin, B. Van, A. Yamada, R. Oyama, M. Sasaki and C. Katan, *Synthesis*, 2017, **49**, 3337–3346.
19 J. Literák, A. Dostálová and P. Klán, *J. Org. Chem.*, 2006, **71**, 713–723.
20 L. Fournier, I. Aujard, T. Le Saux, S. Maurin, S. Beaupierre, J. B. Baudin and L. Jullien, *Chem.–Eur. J.*, 2013, **19**, 17494–17507.
21 Q. Lin, L. Yang, Z. Wang, Y. Hua, D. Zhang, B. Bao, C. Bao, X. Gong and L. Zhu, *Angew. Chem., Int. Ed.*, 2018, **57**, 3722–3726.
22 R. Zhou, L. Yang, Z. Chen, L. Jiang, T. Liu, Z. Wang, X. Huang, Q. Lin, X. Gong, Y. Yang and L. Zhu, *Phys. Chem. Chem. Phys.*, 2023, **25**, 11176–11184.
23 M. Bojtár, A. Kormos, K. Kis-Petik, M. Kellermayer and P. Kele, *Org. Lett.*, 2019, **21**, 9410–9414.
24 J. P. Olson, M. R. Banghart, B. L. Sabatini and G. C. R. Ellis-Davies, *J. Am. Chem. Soc.*, 2013, **135**, 15948–15954.
25 P. Shrestha, K. C. Dissanayake, E. J. Gehrmann, C. S. Wijesooriya, A. Mukhopadhyay, E. A. Smith and A. H. Winter, *J. Am. Chem. Soc.*, 2020, **142**, 15505–15512.
26 A. P. Gorka, R. R. Nani, J. Zhu, S. Mackem and M. J. Schnermann, *J. Am. Chem. Soc.*, 2014, **136**, 14153–14159.
27 G. Alachouzos, A. M. Schulte, A. Mondal, W. Szymanski and B. L. Feringa, *Angew. Chem., Int. Ed.*, 2022, **61**, e202201308.
28 Q. Lin, C. Bao, S. Cheng, Y. Yang, W. Ji and L. Zhu, *J. Am. Chem. Soc.*, 2012, **134**, 5052–5055.
29 Q. Lin, Z. Du, Y. Yang, Q. Fang, C. Bao, Y. Yang and L. Zhu, *Chem.–Eur. J.*, 2014, **20**, 16314–16319.
30 Q. Lin, C. Bao, Y. Yang, Q. Liang, D. Zhang, S. Cheng and L. Zhu, *Adv. Mater.*, 2013, **25**, 1981–1986.
31 Z. Chen, B. Li, X. Xie, F. Zeng and S. Wu, *J. Mater. Chem. B*, 2018, **6**, 2547–2556.
32 M. Bojtár, K. Németh, F. Domahidy, G. Knorr, A. Verkman, M. Kállay and P. Kele, *J. Am. Chem. Soc.*, 2020, **142**, 15164–15171.
33 A. M. Schulte, G. Alachouzos, W. Szymański and B. L. Feringa, *J. Am. Chem. Soc.*, 2022, **144**, 12421–12430.
34 H. D. Nguyen and M. Abe, *J. Am. Chem. Soc.*, 2024, **146**, 10993–11001.
35 R. Schmidt, D. Geissler, V. Hagen and J. Bendig, *J. Phys. Chem. A*, 2007, **111**, 5768–5774.
36 T. Eckardt, V. Hagen, B. Schade, R. Schmidt, C. Schweitzer and J. Bendig, *J. Org. Chem.*, 2002, **67**, 703–710.
37 C. Wang, W. Chi, Q. Qiao, D. Tan, Z. Xu and X. Liu, *Chem. Soc. Rev.*, 2021, **50**, 12656–12678.
38 C. Wang, W. Jiang, D. Tan, L. Huang, J. Li, Q. Qiao, P. Yadav, X. Liu and Z. Xu, *Chem. Sci.*, 2023, **14**, 4786–4795.
39 M. Ojha, M. Banerjee, M. Mandal, T. Singha, S. Ray, P. K. Datta, M. Mandal, A. Anoop and N. D. P. Singh, *ACS Appl. Mater. Interfaces*, 2024, **16**, 21486–21497.
40 S. C. Lee, J. Heo, H. C. Woo, J. A. Lee, Y. H. Seo, C. L. Lee, S. Kim and O. P. Kwon, *Chem.–Eur. J.*, 2018, **24**, 13706–13718.
41 M. A. Haidekker and E. A. Theodorakis, *Org. Biomol. Chem.*, 2007, **5**, 1669–1678.
42 T. Iwaki, C. Torigoe, M. Noji and M. Nakanishi, *Biochemistry*, 1993, **32**, 7589–7592.
43 M. Bojtár, A. Kormos, K. Kis-Petik, M. Kellermayer and P. Kele, *Org. Lett.*, 2019, **21**, 9410–9414.
44 X. Liu, W. Chi, Q. Qiao, S. V. Kokate, E. P. Cabrera, Z. Xu, X. Liu and Y. T. Chang, *ACS Sens.*, 2020, **5**, 731–739.
45 J. Zhang, H. Li, B. Lin, X. Luo, P. Yin, T. Yi, B. Xue, X.-L. Zhang, H. Zhu and Z. Nie, *J. Am. Chem. Soc.*, 2021, **143**, 19317–19329.
46 W. Quan, G. Zhang, L. Huang, W. Song and W. Lin, *J. Mol. Liq.*, 2021, **333**, 115973.
47 Y. Zhang, Z. Li, W. Hu and Z. Liu, *Anal. Chem.*, 2019, **91**, 10302–10309.
48 X. Li, Y. Zhao, J. Yin and W. Lin, *Coord. Chem. Rev.*, 2020, **420**, 213419.
49 X. Gong, R. Guo, X. Li, Y. Yang and W. Lin, *Anal. Methods*, 2024, **16**, 293–300.

50 C. Wan, D. Yang, C. Song, M. Liang, Y. An, C. Lian, C. Dai, Y. Ye, F. Yin, R. Wang and Z. Li, *Chem. Sci.*, 2024, **15**, 5340–5348.
51 A. C. Souza, F. S. Machado, M. R. N. Celes, G. Faria, L. B. Rocha, J. S. Silva and M. A. Rossi, *J. Vet. Med., A*, 2005, **52**, 230–237.
52 M. Millard, J. D. Gallagher, B. Z. Olenyuk and N. Neamati, *J. Med. Chem.*, 2013, **56**, 9170–9179.
53 Y. B. Peng, Z. L. Zhao, T. Liu, G. J. Xie, C. Jin, T. G. Deng, Y. Sun, X. Li, X. X. Hu, X. B. Zhang, M. Ye and W. H. Tan, *ChemMedChem*, 2017, **12**, 250–256.
54 B. Roy, R. Mengji, S. Roy, B. Pal, A. Jana and N. D. P. Singh, *ACS Appl. Mater.*, 2022, **14**, 4862–4870.